ADVANCED MATERIALS

Supporting Information

for *Adv. Mater.*, DOI: 10.1002/adma.201800472

Synthetic Biology Makes Polymer Materials Count

*Hannes M. Beyer, Raphael Engesser, Maximilian Hörner, Julian Koschmieder, Peter Beyer, Jens Timmer, Matias D. Zurbriggen, and Wilfried Weber**

Supporting Information

Synthetic Biology makes Polymer Materials count

Hannes M. Beyer, Raphael Engesser, Maximilian Hörner, Julian Koschmieder, Peter Beyer, Jens Timmer, Matias D. Zurbriggen and Wilfried Weber[*]

Protein Production and Purification:

The plasmids designed for production of the proteins are described in Table S1. All recombinant proteins were produced in strains of *E. coli* BL21 (DE3; Invitrogen). Details are given in Table S2. Cells were harvested by centrifugation at 6,500 x g for 10 min. For recombinant protein purification with Ni^{2+}-NTA resin (refer to Table S2), cells were resuspended in lysis buffer (50 mM NaH_2PO_4, 300 mM NaCl, 10 mM imidazole, pH 8.0) and disrupted using a French Press (APV 2000, APV Manufacturing) at 1,000 bar or by sonication (Bandleine Sonoplus HD3100, 12 min with 60% amplitude and 0.5 s pulse each second). The lysate was clarified by centrifugation at 30,000 x g for 30 min and loaded on a Ni^{2+}-NTA agarose column (Qiagen). After washing (20 column volumes) with lysis buffer and wash buffer (50 mM NaH_2PO_4, 300 mM NaCl, 20 mM imidazole, pH 8.0), the purified protein was eluted (5 column volumes) in elution buffer (50 mM NaH_2PO_4, 300 mM NaCl, 250 mM imidazole, pH 8.0). PIF-CrtI (pHB153) was produced and purified as described previously [1] with the following modifications. In brief, cells were resuspended in CrtI-lysis buffer (50 mM Na_2HPO_4, 300 mM NaCl, 1 mM tris(2-carboxyethyl)phosphine (TCEP), pH 8.0) and disrupted using the French press. The cleared lysate was loaded on Co^{2+}-NTA resin (TALON), washed (20 column volumes) with CrtI-wash buffer (50 mM Na_2HPO_4, 300 mM NaCl, 1 mM TCEP, 4 mM imidazole, pH 8.0) and eluted (5 column volumes) with CrtI-elution buffer (50 mM Na_2HPO_4, 150 mM NaCl, 1 mM TCEP, 150 mM imidazole, pH 8.0). AviTag-TCS-MBP-EK-

CrtY-eGFP-PIF (pHB156) was produced and purified as described previously[2] with the following modifications. In brief, cells were resuspended in CrtY-lysis buffer (100 mM Tris-HCl, 300 mM NaCl, 5 mM $MgCl_2$, 10% glycerol, pH 8.0) and disrupted in the French press. The lysate was clarified by centrifugation at 17,000 x g for 15 min and the supernatant was solubilized with Tween 20 at a 10x critical micellar concentration (CMC, 0.067%) for 30 min on ice, shaking occasionally. The cleared lysate was loaded on Co^{2+}-NTA resin, washed (20 column volume) with CrtY-wash buffer (100 mM Tris-HCl, 300 mM NaCl, 5 mM MgCl2, 4 mM imidazole, 10% glycerol, 0.02% Tween 20, pH 8.0) and finally eluted (5 column volumes) with CrtY-elution buffer (CrtY lysis buffer with 100 mM EDTA and 0.02% Tween 20). The protein was dialyzed against CrtY-dialysis buffer (100 mM Tris-HCl, 300 mM NaCl, 5 mM $MgCl_2$, 10% glycerol, 0.02% Tween 20, pH 6.5), concentrated using Spin-X UF 6 Concentrator 30k MWCO columns (Corning) and stored in aliquots at -80 °C. The proteins were quantified by fluorescence (PhyB/eGFP) or by Bradford assay (Biorad).

Analytical:

The buffers containing the light pulse-counting polymer material were collected, centrifuged (1,500 x g for 1.5 min) and the supernatant (200 µL) was transferred to one well of a black 96-well plate (Corning) prior to measuring the eGFP and mCherry signal with an Infinite M200 pro microplate reader (Tecan) at 488/520 nm and 587/618 nm, respectively. CrtI/CrtY activity was assayed as described elsewhere[1,2] but scaled up (0.9 mL or 1.0 mL assay volume). For measuring CrtY activity, n-hexane (10%) and sodium dithionite (3 mM, Sigma) were added after 6 h CrtI incubation at 37 °C. The reaction was continued for 8 h until carotenoids were extracted using one assay volume of $CHCl_3$/MeOH (2:1). The organic phases were dried and dissolved in $CHCl_3$ (40 µL) for quantification by HPLC analysis using a UFLC XR (Shimadzu) separation module with an SPD-M20A photodiode array detector

and the Labsolutions software. For separation, a YMC-pack-C30 reversed phase column (150 x 3 mm i.d., 5 µm; YMC Europe) and the solvent system A: MeOH/TBME (1:1, v/v) and B: MeOH/H_2O/TBME (30:10:1, v/v/v) were used. The flow rate was 0.6 mL min^{-1} with a gradient from 100% B to 0% B within 20 min and maintenance of the final conditions for four minutes. The column temperature was held at 40 °C. Lycopene and β-carotene were quantified by integrating the peak areas and by normalizing the detector response to a calibration curve made with β-carotene using the extinction coefficients ε_{470} = 185,000 L mol^{-1} cm^{-1} and ε_{450} = 134,000 L mol^{-1} cm^{-1}, respectively.

Zinc staining of the PhyB chromophore phycocyanobilin on SDS-PAGE gels was done by incubation in zinc acetate (1 mM) for 15 min followed by visualization with UV light at 313 nm using an Intas GDS agarose imaging system.

TEV activity was determined using the SensoLyte 520 TEV protease assay kit (AnaSpec) according to the instructions of the manufacturer.

Statistics:

If not indicated otherwise, mean values are shown for at least triplicates with error bars representing +/- one standard error of the mean. Fluorescent signals were normalized to the highest mean value of each group. In Figure 2 the fluorescent values were normalized to the maximum value of the fit-curves in each group. See also below for the error model used in model calibration.

Mathematical Modeling of the Light Pulse-Counting Materials

In the following, the mathematical model describing the light pulse counting material is derived. We modeled the system as a biochemical reaction network with nonlinear ordinary

differential equations (ODE), based on mass action kinetics. The dynamical states of the model represent the concentrations of the involved molecules. First, we derived a core model of the light-induced PhyB-PIF interaction. With this, we next developed a model for the PIF-TEV and a model for OUT-containing materials, connected in a modular manner. Spatial diffusion effects through the polymer membrane (Figure S1) were captured by a compartmentalization strategy. The final model was calibrated by a multi-experiment fit to the data shown in Figure 2 using a maximum likelihood approach that minimizes the distance between the simulated model trajectories and the data of all experiments simultaneously. Parameter uncertainties and the system identifiability were analyzed using an approach based on the profile likelihood.

Core Model of the Light-Induced PhyB-PIF Interaction

The red light-sensing photoreceptor phytochrome B has two conformations, the far-red light (740 nm)-sensing $PhyB_{FR}$ state and the red light (660 nm)-sensing $PhyB_R$ state. $PhyB_{FR}$ can bind to the phytochrome-interacting factor 6 (PIF), while illumination with 740 nm light leads to a transition to $PhyB_R$, incapable of binding to PIF (Figure S5a). Since the absorption spectra of $PhyB_{FR}$ and $PhyB_R$ overlap ([3], Figure S2d-e), PhyB is always present in both conformations, with a fraction of PhyB bound to PIF. To take this into account, one must describe the light-induced transformation change of PhyB and the binding and dissociation of PhyB/PIF by two independent processes (Figure S5b). The light-induced conformation change of PhyB is modeled by the rate constants $k_{on}(\lambda)$ and $k_{off}(\lambda)$, depending on the used wavelength λ. The PhyB/PIF complex can only be formed with $PhyB_{FR}$. The dissociation of PhyB/PIF is only possible in the $PhyB_R$ state.

Using mass action kinetics, we obtain the ODE system:

$$\frac{d}{dt}[PIF] = -k_{form}[PIF][PhyB_{FR}] + k_{diss}[PhyB_R\_PIF] \tag{1.1}$$

$$\frac{d}{dt}[PhyB_{FR}] = -k_{form}[PIF][PhyB_{FR}] - k_{on}(\lambda)[PhyB_{FR}] + k_{off}(\lambda)[PhyB_R] \tag{1.2}$$

$$\frac{d}{dt}[PhyB_R] = k_{diss}[PhyB_R\_PIF] + k_{on}(\lambda)[PhyB_{FR}] - k_{off}(\lambda)[PhyB_R] \tag{1.3}$$

$$\frac{d}{dt}[PhyB_{FR}\_PIF] = k_{form}[PIF][PhyB_{FR}] - k_{on}(\lambda)[PhyB_{FR}\_PIF] + k_{off}(\lambda)[PhyB_R\_PIF] \tag{1.4}$$

$$\frac{d}{dt}[PhyB_R\_PIF] = -k_{diss}[PhyB_R\_PIF] + k_{on}(\lambda)[PhyB_{FR}\_PIF] - k_{off}(\lambda)[PhyB_R\_PIF]. \tag{1.5}$$

Since the light-induced conformation change of PhyB is orders of magnitudes faster than the time scale of the formation and dissociation of PhyB/PIF, we can assume this reaction to be in a quasi steady state. With the law of mass action, we obtain

$$\frac{[PhyB_{FR}]}{[PhyB_R]} = \frac{[PhyB_{FR}\_PIF]}{[PhyB_F\_PIF]} = \frac{k_{off}(\lambda)}{k_{on}(\lambda)} = K_{eq}(\lambda). \tag{1.6}$$

$PhyB_{FR}$ and $PhyB_{FR}$_PIF are proportional to $PhyB_R$ and $PhyB_R$_PIF, respectively. A change in the concentration of one state is instantly translated into a change of the other state. This can be used to reduce the ODE system (1.1)–(1.5) by taking the sum of equations (1.2)+(1.3) and of equations (1.4)+(1.5). By using the relations $[PhyB_{FR}] = K_{eq}(\lambda)[PhyB_R]$ and $[PhyB_{FR}PIF] = K_{eq}(\lambda)[PhyB_R\_PIF]$ we can substitute the derivatives of [$PhyB_{FR}$] and [$PhyB_{FR}$_PIF] and obtain the reduced system

$$\frac{d}{dt}[PIF] = -k_{form}[PIF][PhyB_{FR}] + k_{diss}[PhyB_R\_PIF] \tag{1.7}$$

$$\frac{d}{dt}[PhyB_R] = \frac{-k_{form}[PIF][PhyB_{FR}] + k_{diss}[PhyB_R\_PIF]}{1 + K_{eq}(\lambda)} \tag{1.8}$$

$$\frac{d}{dt}[PhyB_R\_PIF] = \frac{k_{form}[PIF][PhyB_{FR}] - k_{diss}[PhyB_R\_PIF]}{1 + K_{eq}(\lambda)}, \quad (1.9)$$

with $[PhyB_{FR}] = K_{eq}(\lambda)[PhyB_R]$ and $[PhyB_{FR}\_PIF] = K_{eq}(\lambda)[PhyB_R\_PIF]$.

According to Mancinelli[3], the equilibrium constant is $K_{eq}(\lambda=660\ nm)=6.67$ for 660 nm and $K_{eq}(\lambda=740\ nm)=0.0167$ for 740 nm.

Modeling PIF-TEV and the OUT materials subsystems

Using the core model of the light-induced PhyB/PIF binding, we can derive the models for the PIF-TEV and OUT materials subsystems. The PIF-TEV subsystem consists of the PIF-TEV protein, which can bind to polymer-bound PhyB. This means, for the time-delay device, we can use the core model with the states:

- $PhyB_{FR}$ PhyB in the $PhyB_{FR}$ form attached to a polymer
- $PhyB_R$ PhyB in the $PhyB_R$ form attached to a polymer
- PIF_TEV Free PIF-TEV
- $PhyB_{FR}$_PIF_TEV PIF-TEV bound to the $PhyB_{FR}$ form of PhyB
- $PhyB_R$_PIF_TEV PIF-TEV bound to the $PhyB_R$ form of PhyB

In the OUT subsystem, the output protein eGFP is fused to PIF and to a TEV cleavage site (TCS) with a biotinylation motif that can bind to the streptavidin-functionalized polymer. This leads to the states of the OUT subsystem:

- $PhyB_{FR}$ PhyB in the $PhyB_{FR}$ form attached to a polymer

- $PhyB_R$ PhyB in the $PhyB_R$ form attached to a polymer
- PIF_eGFP Free PIF_eGFP with cleaved TCS
- $PhyB_{FR}$_PIF_eGFP_TCS eGFP bound to $PhyB_{FR}$ with intact TCS
- $PhyB_{FR}$_PIF_eGFP eGFP bound to the $PhyB_{FR}$ form with cleaved TCS
- $PhyB_R$_PIF_eGFP_TCS eGFP bound to $PhyB_R$ with intact TCS
- $PhyB_R$_PIF_eGFP eGFP bound to the $PhyB_R$ form with cleaved TCS

The states $PhyB_{FR}$_eGFP_TCS and $PhyB_R$_eGFP_TCS with a intact TCS but free PIF are neglected because eGFP is still bound to the polymer and the PIF binding is, therefore, only a conformation change that happens on a very fast time scale. The cleavage of the TCS corresponds to a switch of a memory event which is achieved by free PIF_TEV from the PIF-TEV subsystem to cleave the TCS. We also included a basal TCS cleavage rate due to instabilities of the molecular bonds and to describe the leakiness of the system.

By connecting both systems, one obtains the basic reactions:

- Light induced conformation changes:

$$PhyB_R\_X \underset{k_{on}(\lambda)}{\overset{k_{off}(\lambda)}{\rightleftarrows}} PhyB_{FR}\_X \tag{1.10}$$

- PhyB-PIF interaction:

$$PhyB_R\_PIF\_eGFP \xrightarrow{k_{diss\_eGFP}} PhyB_R + PIF\_eGFP \tag{1.11}$$

$$PhyB_R\_PIF\_TEV \xrightarrow{k_{diss\_TEV}} PhyB_R + PIF\_TEV \tag{1.12}$$

$$PhyB_{FR} + PIF\_eGFP \xrightarrow{k_{form}} PhyB_{FR}\_PIF\_eGFP \tag{1.13}$$

$$PhyB_{FR} + PIF\_TEV \xrightarrow{k_{form}} PhyB_{FR}\_PIF\_TEV \tag{1.14}$$

- TCS cleavage by PIF_TEV:

$$PhyB_R\_PIF\_eGFP\_TCS \xrightarrow{k_{cut\_basal}+k_{cut\_TEV}[PIF\_TEV]} PhyB_R\_PIF\_eGFP \quad (1.15)$$

$$PhyB_{FR}\_PIF\_eGFP\_TCS \xrightarrow{k_{cut\_basal}+k_{cut\_TEV}[PIF\_TEV]} PhyB_{FR}\_PIF\_eGFP \quad (1.16)$$

For the dissociation of $PhyB_R$_PIF_eGFP and $PhyB_R$_PIF_TEV, we used different dissociation rates since it is unclear whether the additionally fused TCS influences the chemical properties of the PhyB/PIF interaction. Additionally, different protein sizes may lead to varying diffusion rates out of the polymer material. To avoid over-fitting, the same value for the formation rate k_{form} was chosen for the formation of both $PhyB_{FR}$_PIF_eGFP and $PhyB_{FR}$_PIF_TEV.

This system was translated to ODE using mass action kinetics. The transition between all $PhyB_{FR}$ forms and their corresponding $PhyB_R$ form is described with quasi steady states, as shown in the derivation of the core model. The reduction of the model was again performed by addition of the two ODEs describing $PhyB_R$_X and the corresponding $PhyB_{FR}$_X and using the proportionality of the two PhyB forms $[PhyB_{FR}\_X] = K_{eq}(\lambda)[PhyB_R\_X]$. With this, one obtains the rates

$$v1 = k_{form}[PIF\_TEV][PhyB_{FR}] \quad (1.17)$$

$$v2 = k_{diss\_TEV}[PhyB_R\_PIF\_TEV] \quad (1.18)$$

$$v3 = k_{form}[PIF\_eGFP][PhyB_{FR}] \quad (1.19)$$

$$v4 = k_{diss\_eGFP}[PhyB_R\_PIF\_eGFP] \quad (1.20)$$

$$v5 = k_{cut\_basal}[PhyB_R\_PIF\_eGFP\_TCS] + k_{cut\_TEV}[PIF\_TEV][PhyB_R\_PIF\_eGFP\_TCS] \quad (1.21)$$

forming the following ODE system

$$\frac{d}{dt}[PIF\_TEV] = -v1 + v2 \tag{1.22}$$

$$\frac{d}{dt}[PIF\_eGFP] = -v3 + v4 \tag{1.23}$$

$$\frac{d}{dt}[PhyB_R] = \frac{-v1 + v2 - v3 + v4}{1 + K_{eq}(\lambda)} \tag{1.24}$$

$$\frac{d}{dt}[PhyB_R\_PIF\_TEV] = \frac{v1 - v2}{1 + K_{eq}(\lambda)} \tag{1.25}$$

$$\frac{d}{dt}[PhyB_R\_PIF\_eGFP] = \frac{v3 - v4 + v5}{1 + K_{eq}(\lambda)} \tag{1.26}$$

$$\frac{d}{dt}[PhyB_R\_PIF\_eGFP\_TCS] = \frac{-v5}{1 + K_{eq}(\lambda)} \tag{1.27}$$

with

$$[PhyB_{FR}] = K_{eq}(\lambda)[PhyB_F] \tag{1.28}$$

$$[PhyB_{FR}\_PIF\_TEV] = K_{eq}(\lambda)[PhyB_R\_PIF\_TEV] \tag{1.29}$$

$$[PhyB_{FR}\_PIF\_eGFP] = K_{eq}(\lambda)[PhyB_R\_PIF\_eGFP] \tag{1.30}$$

$$[PhyB_{FR}\_PIF\_eGFP\_TCS] = K_{eq}(\lambda)[PhyB_R\_PIF\_eGFP\_TCS]. \tag{1.31}$$

Combing the Models Using a Compartmentalization Strategy

For the experimental implementation of the light pulse counting material, we separated the polymer material with PIF_TEV load from the material with PIF_eGFP load to ensure diffusion and prevent TCS cleavage due to unintended contact of bound PIF_eGFP with polymer bound PIF_TEV. To model this, we chose a compartmentalization strategy with three spatially separated compartments C1, C2 and C3. Since the polymer material is immobile, only free PIF_TEV and PIF_eGFP is able to pass between the three compartments. C1 contains the PIF-TEV subsystem with the PIF_TEV loaded polymer and compartment C3

contains the OUT subsystem. The compartment C2 consists of buffer. Since PIF_TEV and PIF_eGFP can pass between the compartments in both C1 and C3, PhyB/PIF complexes with PIF_TEV and PIF_eGFP are possible. The complexes with uncleaved TCS $PhyB_{FR}$_PIF_eGFP_TCS and $PhyB_R$_PIF_eGFP_TCS can only exist in compartment C3 (Figure S5c). The transition between the three compartments is modelled by the reactions

$$PIF\_TEV\_C1 \underset{k_{c2c1}}{\overset{k_{c1c2}}{\rightleftarrows}} PIF\_TEV\_C2 \tag{1.32}$$

$$PIF\_TEV\_C2 \underset{k_{c3c2}}{\overset{k_{c2c3}}{\rightleftarrows}} PIF\_TEV\_C3 \tag{1.33}$$

$$PIF\_eGFP\_C1 \underset{k_{c2c1}}{\overset{k_{c1c2}}{\rightleftarrows}} PIF\_eGFP\_C2 \tag{1.34}$$

$$PIF\_eGFP\_C2 \underset{k_{c3c2}}{\overset{k_{c2c3}}{\rightleftarrows}} PIF\_eGFP\_C3, \tag{1.35}$$

e.g. the transition from the compartment C1 to C2 is proportional to the rate constant k_{c1c2}. The transition rates between the polymer-loaded compartments C1/C3 and C2 can be unequal. Reasons are differences in the viscosity of the polymer and buffer, but also deliquescence effects of the polymer, leading to lower diffusion rates into the polymer.

By copying the states of the ODE system (1.22)–(1.27) to the three compartments and including the transition rates between the compartments, we obtain following rates

$$v1 = k_{form}[PIF\_TEV\_C3][PhyB_{FR}\_C3] \tag{1.36}$$

$$v2 = k_{diss\_TEV}[PhyB_R\_PIF\_TEV\_C3] \tag{1.37}$$

$$v3 = k_{form}[PIF\_eGFP\_C3][PhyB_{FR}\_C3] \tag{1.38}$$

$$v4 = k_{diss\_eGFP}[PhyB_R\_PIF\_eGFP\_C3] \tag{1.39}$$

$$v5 = k_{cut\_basal}[PhyB_R\_PIF\_eGFP\_TCS\_C3] + k_{cut\_TEV}[PIF\_TEV\_C3][PhyB_R\_PIF\_eGFP\_TCS\_C3] \tag{1.40}$$

$$v6 = k_{form}[PIF\_TEV\_C1][PhyB_{FR}\_C1] \tag{1.41}$$

$$v7 = k_{diss\_TEV}[PhyB_R\_PIF\_TEV\_C1] \tag{1.42}$$

$$v8 = k_{form}[PIF\_eGFP\_C1][PhyB_{FR}\_C1] \tag{1.43}$$

$$v9 = k_{diss\_eGFP}[PhyB_R\_PIF\_eGFP\_C1] \tag{1.44}$$

$$v10 = k_{C3C2}[PIF\_TEV\_C3] - k_{C2C3}[PIF\_TEV\_C2] \tag{1.45}$$

$$v11 = k_{C1C2}[PIF\_TEV\_C1] - k_{C2C1}[PIF\_TEV\_C2] \tag{1.46}$$

$$v12 = k_{C3C2}[PIF\_eGFP\_C3] - k_{C2C3}[PIF\_eGFP\_C2] \tag{1.47}$$

$$v13 = k_{C1C2}[PIF\_eGFP\_C1] - k_{C2C1}[PIF\_eGFP\_C2] \tag{1.48}$$

which are forming the final ODE model of the light pulse counting materials system:

Compartment C3:

$$\frac{d}{dt}[PIF\_TEV\_C3] = -v1 + v2 - v10 \tag{1.49}$$

$$\frac{d}{dt}[PIF\_eGFP\_C3] = -v3 + v4 - v12 \tag{1.50}$$

$$\frac{d}{dt}[PhyB_R\_C3] = \frac{-v1 + v2 - v3 + v4}{1 + K_{eq}(\lambda)} \tag{1.51}$$

$$\frac{d}{dt}[PhyB_R\_PIF\_TEV\_C3] = \frac{v1 - v2}{1 + K_{eq}(\lambda)} \tag{1.52}$$

$$\frac{d}{dt}[PhyB_R\_PIF\_eGFP\_C3] = \frac{v3 - v4 + v5}{1 + K_{eq}(\lambda)} \tag{1.53}$$

$$\frac{d}{dt}[PhyB_R\_PIF\_eGFP\_TCS\_C3] = \frac{-v5}{1 + K_{eq}(\lambda)} \tag{1.54}$$

Compartment C1:

$$\frac{d}{dt}[PIF\_TEV\_C1] = -v6 + v7 - v11 \tag{1.55}$$

$$\frac{d}{dt}[PIF\_eGFP\_C1] = -v8 + v9 - v13 \tag{1.56}$$

$$\frac{d}{dt}[PhyB_R\_C1] = \frac{-v6 + v7 - v8 + v9}{1 + K_{eq}(\lambda)} \tag{1.57}$$

$$\frac{d}{dt}[PhyB_R\_PIF\_TEV\_C1] = \frac{v6 - v7}{1 + K_{eq}(\lambda)} \tag{1.58}$$

$$\frac{d}{dt}[PhyB_R\_PIF\_eGFP\_C1] = \frac{v8 - v9}{1 + K_{eq}(\lambda)} \tag{1.59}$$

Compartment C2:

$$\frac{d}{dt}[PIF\_TEV\_C2] = v10 + v11 \tag{1.60}$$

$$\frac{d}{dt}[PIF\_eGFP\_C2] = v12 + v13. \tag{1.61}$$

As described above the concentration of the complexes containing the $PhyB_{FR}$ form is

$$[PhyB_{FR}\_X] = K_{eq}(\lambda)[PhyB_R\_X]. \tag{1.62}$$

Maximum Likelihood Approach and Identifiability Analysis

The ODE system (1.49)–(1.61) can be written in the general form,

$$\frac{d}{dt}\vec{x}(t) = \vec{f}\left(\vec{x}, \vec{p}, \vec{u}(t)\right) \tag{1.63}$$

with the state vector $\vec{x}(t) \in \mathbb{R}^n$ describing the temporal evolution of the concentrations of the modeled proteins, $\vec{p} \in \mathbb{R}^{n_p}$ is a vector containing the dynamic parameters, e.g. the biochemical rate constants. The function $\vec{u}(t) \in \mathbb{R}^{n_u}$ contains external inputs, i.e. the light conditions, which can change over time. To solve the ODE system, one also needs initial conditions $\vec{x}(0) = \vec{x}_0 \in \mathbb{R}^n$.

To link the model states $\vec{x}(t)$ to the measured data $y(t)$, we define the observation function

$$y(t) = g(\vec{x}(t), \vec{s}) + \varepsilon(t), \tag{1.64}$$

with the observation parameters $\vec{s} \in \mathbb{R}^{n_s}$, e.g. scaling or offset parameters. The measurement error $\varepsilon(t)$ is modelled by a constant Gaussian error with variance σ^2:

$$\varepsilon(t) \sim N(0, \sigma^2). \tag{1.65}$$

With this, we can write down the probability of a measured data set $\vec{y}^D$ given by a parameter vector $\vec{\theta} = (\vec{p}, \vec{x}_0, \vec{s}, \sigma)$ as

$$L(\vec{y}^D, \vec{\theta}) = \prod_{j=1}^{N_D} \exp\left(\frac{\left(y_j^D - g(\vec{x}(t_j), \vec{s}) \right)^2}{2\sigma^2} \right). \tag{1.66}$$

N_d denotes the number of data points and t_j are the time points of measurement. For multiple experiments, the total probability is the product of the probabilities of the single experiments:

$$L(\vec{y}^D, \vec{\theta}) = \prod_{k=1}^{N_{\text{exp}}} L(\vec{y}^{D_k}, \vec{\theta}_k). \tag{1.67}$$

$L(\vec{y}^D, \vec{\theta})$ seen as function of the parameters $\vec{\theta}$ given the data $\vec{y}^D$ is called a likelihood function. The maximum likelihood estimator $\hat{\theta}$ of the parameter set $\vec{\theta}$ is then defined as

$$\hat{\theta} = \arg\max_{\theta}\left(L(\vec{y}^{D},\vec{\theta})\right). \tag{1.68}$$

Instead of maximizing the likelihood L, it is equivalent to take the minimum of

$$-2\log L = \sum_{j=1}^{N_D}\left(\frac{y_j^D - g(\vec{x}(t_j),\vec{s})}{\sigma}\right)^2 + 2N_D\log\left(\sqrt{2\pi}\sigma\right) =: \chi^2_{\mathrm{mod}}(\vec{\theta}) \tag{1.69}$$

which is just the sum of the weighted squared residuals $\chi^2(\vec{\theta}) = \sum_{j=1}^{N_D}\left(\frac{y_j^D - g(\vec{x}(t_j),\vec{s})}{\sigma}\right)^2$ with an additional term due to the error model. The optimal parameter set $\hat{\theta}$ is then obtained by

$$\hat{\theta} = \arg\min_{\theta}\left(\chi^2_{\mathrm{mod}}(\vec{\theta})\right). \tag{1.70}$$

To quantify parameter uncertainties in terms of parameter confidence intervals and to analyze parameter identifiabilities, we calculated the profile likelihood[4] for each parameter θ_i

$$\chi^2_{PL}(\theta_i) = \min_{\theta_{i\neq j}}\chi^2_{\mathrm{mod}}(\vec{\theta}). \tag{1.71}$$

With this, one can calculate the 95 % parameter confidence intervals with

$$CI(\theta_i) = \left\{\theta \,|\, \chi^2(\theta) - \chi^2(\hat{\theta}) < \chi^2(95\%, df = 1)\right\}. \tag{1.72}$$

$\chi^2(\alpha, df)$ is the α-quantile of the χ^2-distribution with df degrees of freedom.

Implementation of the Single Experiments

In the following, the implementation of the single experiments shown in Figure 2 is described and the corresponding observation functions are defined. If not stated otherwise, the initial concentrations of all states were set to zero.

Experiment 1: Characterization of the PIF-TEV subsystem

In this experiment (shown in Figure 2a), we tested the PIF-TEV subsystem. We used only polymer material loaded with PIF-TEV in the compartment C1 and measured the release of PIF-TEV under illumination with 660 and 740 nm light. As the observation function we used the total amount of free PIF_TEV

$$mCherry\_obs = scale_{TEV\_Exp1}\left([PIF\_TEV\_C1]+[PIF\_TEV\_C2]+[PIF\_TEV\_C3]\right). \quad (1.73)$$

Initially, we assumed that all PIF_TEV is bound to PhyB. Additionally, empty functional material with PhyB attached was added. Hence, we set the initial conditions:

$$[PhyB_R\_PIF\_TEV\_C1](0) = init_{Exp13} / (1 + K_{eq}(\lambda)) \quad (1.74)$$

$$[PhyB_R\_C1](0) = 0.5 \cdot init_{Exp13} / (1 + K_{eq}(\lambda)). \quad (1.75)$$

With $[PhyB_{FR}\_PIF\_TEV\_C1](0) = K_{eq}(\lambda)[PhyB_R\_PIF\_TEV\_C1](0)$ follows

$$[PhyB_{FR}\_PIF\_TEV\_C1](0) + [PhyB_R\_PIF\_TEV\_C1](0) = init_{Exp13}. \quad (1.76)$$

The parameter initExp13 corresponds to the concentration of the bound PIV_TEV in C1.

Experiment 2: Characterization of the OUT Subsystem

In this experiment (shown in Figure 2b), we characterized the OUT subsystem by inducing the release of the output by addition of different concentrations of PIF_TEV under illumination with 660 and 740 nm light. We used only polymer material loaded with PIF_eGFP in compartment C3. As the observation function we used

$$eGFP\_obs = scale_{EGFP\_Exp2}\left([PIF\_eGFP\_C1]+[PIF\_eGFP\_C2]+[PIF\_eGFP\_C3]\right). \quad (1.77)$$

As initial concentrations, we chose

$$[PhyB_R\_PIF\_eGFP\_TCS\_C3](0) = init_{Exp2}/(1+K_{eq}(\lambda)) \quad (1.78)$$

$$[PhyB_R\_C3](0) = 0.5\cdot init_{Exp2}/(1+K_{eq}(\lambda)) \quad (1.79)$$

$$[PIF\_TEV\_c2](0) = TEV\_input. \quad (1.80)$$

The parameter init_Exp2 is the concentration of bound PIF_eGFP in C3. The parameter TEV_input was set to the amount of PIF-TEV added to the system.

Experiment 3: Characterization of the Full System

In this experiment (shown in Figure 2c-d), we implemented both the PIF-TEV and the OUT subsystem. In compartment C1, we added polymer with PIF-TEV and, in compartment C3, polymer material loaded with PIF_eGFP.

As observation functions, we used

$$eGFP\_obs = scale_{EGFP\_Exp3}\left([PIF\_eGFP\_C1]+[PIF\_eGFP\_C2]+[PIF\_eGFP\_C3]\right) \quad (1.81)$$

$$mCherry\_obs = scale_{TEV\_Exp3}\left([PIF\_TEV\_C1]+[PIF\_TEV\_C2]+[PIF\_TEV\_C3]\right). \quad (1.82)$$

The initial concentrations were set to

$$[PhyB_R\_PIF\_TEV\_C1](0) = init_{Exp13} / (1 + K_{eq}(\lambda(0))) \quad (1.83)$$

$$[PhyB_R\_C1](0) = 0.5 \cdot init_{Exp13} / (1 + K_{eq}(\lambda(0))) \quad (1.84)$$

$$[PhyB_R\_PIF\_eGFP\_TCS\_C3](0) = init_{Exp13} / (1 + K_{eq}(\lambda(0))) \quad (1.85)$$

$$[PhyB_R\_C3](0) = 0.5 \cdot init_{Exp13} / (1 + K_{eq}(\lambda(0))). \quad (1.86)$$

After 240 minutes, the light conditions were switched, meaning that $\lambda(t)$ is a time dependent input function. Besides changing $K_{eq}(\lambda(t))$, one must also reset the ratio of $PhyB_{FR}$ to $PhyB_R$ to assure mass conservation.

Fitting Results

The model with the observation functions was fitted to the data shown in Figure 2 using maximum likelihood estimation. In total, 19 parameters were fitted, of which nine were dynamic parameters, two initial parameters, four scaling parameters and four error parameters.

For the numerical integration, fitting process and profile likelihood analysis, we used the MATLAB based freely available Data2Dynamics software[5]. Numerical integration of the ODE system was done with the CVODES[6] solver with optimization being done with a trust region based algorithm (LSQNONLIN) implemented in MATLAB[7]. The parameter sensitivities were calculated by solving the sensitivity equations of the system.

In order to scan the parameters over orders of magnitude and to improve convergence, we fitted in logarithmic parameter space. To ensure global convergence of the optimizer, we performed multiple optimization runs with random sampled initial parameter sets. From a total of 500 runs, 147 converged to the same lowest minimum, indicating that this is the global minimum (Figure S6). However, other local minima were found. Because their –2log(L) value is statistically significantly worse, these minima were not considered in the further analysis. The fitted parameter values are shown in Table S3. The resulting model curves describing the experiments are shown in Figure 2. The shaded error bands represent the estimated standard deviation σ of the used error model.

The identifiability analysis with the profile likelihood shows that all parameters except k_{c2c3} and k_{c3c2} are identifiable (Figure S7a). The parameters k_{c2c3} and k_{c3c2} are practical non-identifiable to +infinity. To test the influence of this non-identifiability on the predictions shown in Figure 2e and 3b, we simulated all parameter sets along the profiles of k_{c2c3} and k_{c3c2}. This can be used to translate the uncertainty of the parameter estimate to the uncertainty of the prediction[8]. The analysis reveals that the practical non-identifiability of k_{c2c3} and k_{c3c2} has no effect on the model predictions in Figure 2e and 3b and, therefore, has no influence on the predictive power of the model. Furthermore, the non-identifiability has no effect on predictions where the observation function is the sum of all three compartments. The 95 % point-wise confidence intervals calculated with equation (1.72) are shown in Table S3.

Prediction of the Counting Characteristics and Experimental Validation of the Model

In this section, we describe the validation analysis of Figure 2e by testing the statistical agreement of the validation experiment with the model prediction by exploiting the prediction profile likelihood and the validation profile likelihood.

As a measure for the counting properties of the system, we chose the ratio of the output signal after two 740 nm light pulses versus the signal obtained after only one single light

pulse of double duration to keep the total 740 nm illumination period identical. In contrast to simply comparing the signal after two pulses to the signal after one pulse of the same length, a system that is just integrating the input signal over time, is not assumed to be counting. Additionally, the system is only defined as being able to count when the signal obtained by two pulses is higher than the basal output of the system (represented by the output signal in the absence of any 740 nm light pulse). This is ensured by taking the ratio

$$r = \frac{Signal\ after\ two\ pulses}{\max(Signal\ after\ one\ long\ pulse\ ,\ basal\ activation)}. \tag{1.87}$$

The prediction of the ratio r was performed by using the mathematical model with the estimated optimal parameter set $\hat{\theta}$ and simulate the system response for the combinations of pulse duration and pause as depicted in Figure 2e. The uncertainties of the estimated parameter values $\hat{\theta}$ are leading to uncertainties in the simulated predictions. To quantitatively determine these uncertainties in terms of prediction confidence intervals, we calculated the prediction profile likelihood[9] for each ratio, which was experimentally validated. The result is shown in Figure S7b. The 95% point-wise prediction confidence intervals are shown in Table S4.

To validate the predictions with experimental data, we measured selected points with different combinations of the pulse length and pause between two pulses (Figure 2e circles, Figure 2f). The experimental results are shown in Table S5. The depicted error was obtained by propagating the standard error of the mean of the measured triplicates. To test the agreement of the validation experiment with the model prediction, one must consider the confidence interval of the prediction and the error of the validation measurement. This is done by the validation profile likelihood, which incorporates sources of uncertainty, the prediction

uncertainty and the measurement error[9]. The validation profile likelihood of the four predictions is shown in Figure S7c and the 95% point-wise validation confidence intervals are given in Table S4. The calculation of the prediction and validation profile likelihood was done with the doPPL plugin for the Data2dynamics software package[10].

This analysis revealed that all measured validation experiments are in their corresponding 95% validation confidence interval and therefore, confirmed the predictive power of the model.

Dependence of the optimal pulse length on diffusion

The calibrated model can be utilized to analyze the properties of the system and to identify parameters to tune the characteristics of the system. In this section, this is exemplarily shown for the length of the applied light pulses. In a model-based approach we identify possible modifications of the system to obtain different optimal pulse lengths in terms of the capability of the system for counting.

As described in the previous section, the counting property of the system can be quantified with the measure

$$r = \frac{Signal\ after\ two\ pulses}{\max(Signal\ after\ one\ long\ pulse\ ,\ basal\ activation)}, \tag{1.87}$$

which has to be greater than one to be in the counting regime. As Figure 2e shows, the general property of the system to count is very robust when changing the length of the light pulses. However, there is a region in which we obtain optimal counting properties, which are at pulse lengths from 20 to 40 minutes depending on the time between the pulses. The question is now, if it is possible to modify the system to obtain different optimal pulse lengths. Using a model-based simulation study, we identified the time scale of the TEV subsystem to correlate with

the pulse length. This time scale depends on the time TEV needs to reach its cleavage site. This corresponds directly to the diffusion speed of TEV between the three compartments in the system. With the calibrated model it is possible to perform simulations with changing transition rates between the compartments mimicking a change in the diffusion. Figure S8 shows such simulations in which we calculated the ratio *r* for different pulse lengths and different scalings of the diffusion between the three compartments. This was implemented by multiplying all transition rates between the compartments by a fold change factor, which is denoted on the x-axis of Figure S8.

The resulting simulation shows a strong negative correlation between the optimal pulse lengths with the change of the diffusion speed. This suggests, by changing the diffusion speed, it is possible to adjust the optimal pulse length from the scale of minutes to hours.

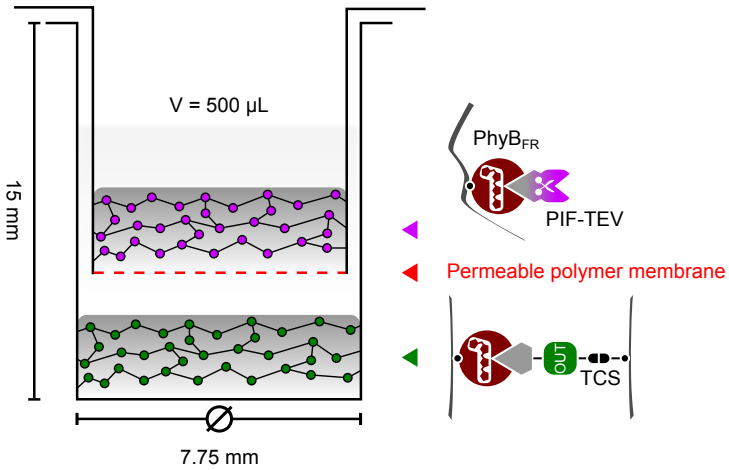

Figure S1. Experimental configuration of the light pulse-counting materials system. The modular material building blocks comprising the OUT and PIF-TEV modules were combined in one materials system. A diffusion-based TCS cleavage mechanism was implemented by separating the modules by a permeable polymer membrane (20 µm mesh size).

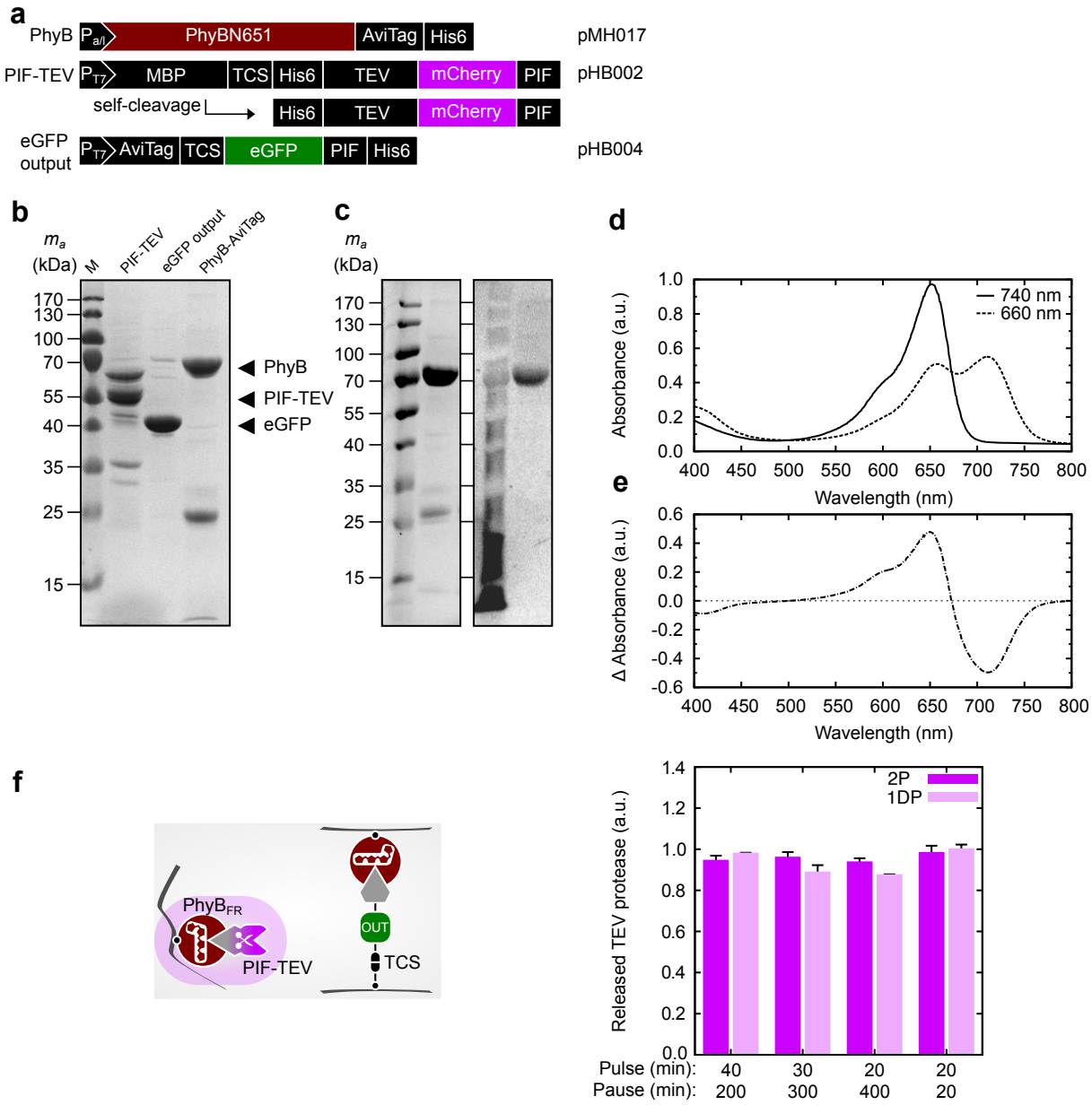

Figure S2. Synthesis and characterization of the building blocks. **a**, Schematic representation of the expression vectors for the synthesis of the protein building blocks. Note PIF-TEV harboring a TCS results in self-cleavage during production *in vivo*, see Table S1 for full description. **b**, Coomassie staining of the Ni^{2+}-NTA-purified fluorescent building blocks PIF-TEV, eGFP output protein, and PhyB-AviTag after SDS-PAGE. **c**, Coomassie and zinc staining of PhyB-AviTag. 0.7 mg Ni^{2+}-NTA eluted PhyB-AviTag was incubated with 10 µL streptavidin-functionalized agarose (2.4 nmol biotin-binding capacity) at 4 °C under rotation. The immobilized protein was washed with lysis buffer and subjected to SDS-PAGE, coomassie staining, and zinc staining (to visualize the bound chromophore PCB). **d**, Spectral characterization of Ni^{2+}-NTA purified biotinylated PhyB-AviTag after 5 min of exposure to 660 or 740 nm light. **e**, Difference absorption spectrum of 740 – 660 nm light illuminated PhyB. **f**, Evaluation of PIF-TEV release from the complete counting materials system (left panel). The system was subjected to the indicated illumination regimes. The release of PIF-TEV was quantified by determining the fluorescence of the mCherry linker joining PIF and TEV. Mean values of at least three replicates +/- s.e.m. are shown. Abbreviations: AviTag, biotinylation motif; His6, hexahistidine-tag; MBP, maltose-binding protein; PCB,

phycocyanobilin; PhyBN651, N-terminal fragment of Arabidopsis phytochrome B comprising amino acid residues 1-651; PIF, phytochrome interacting factor 6 amino acid residues 1-100; TCS, TEV cleavage site.

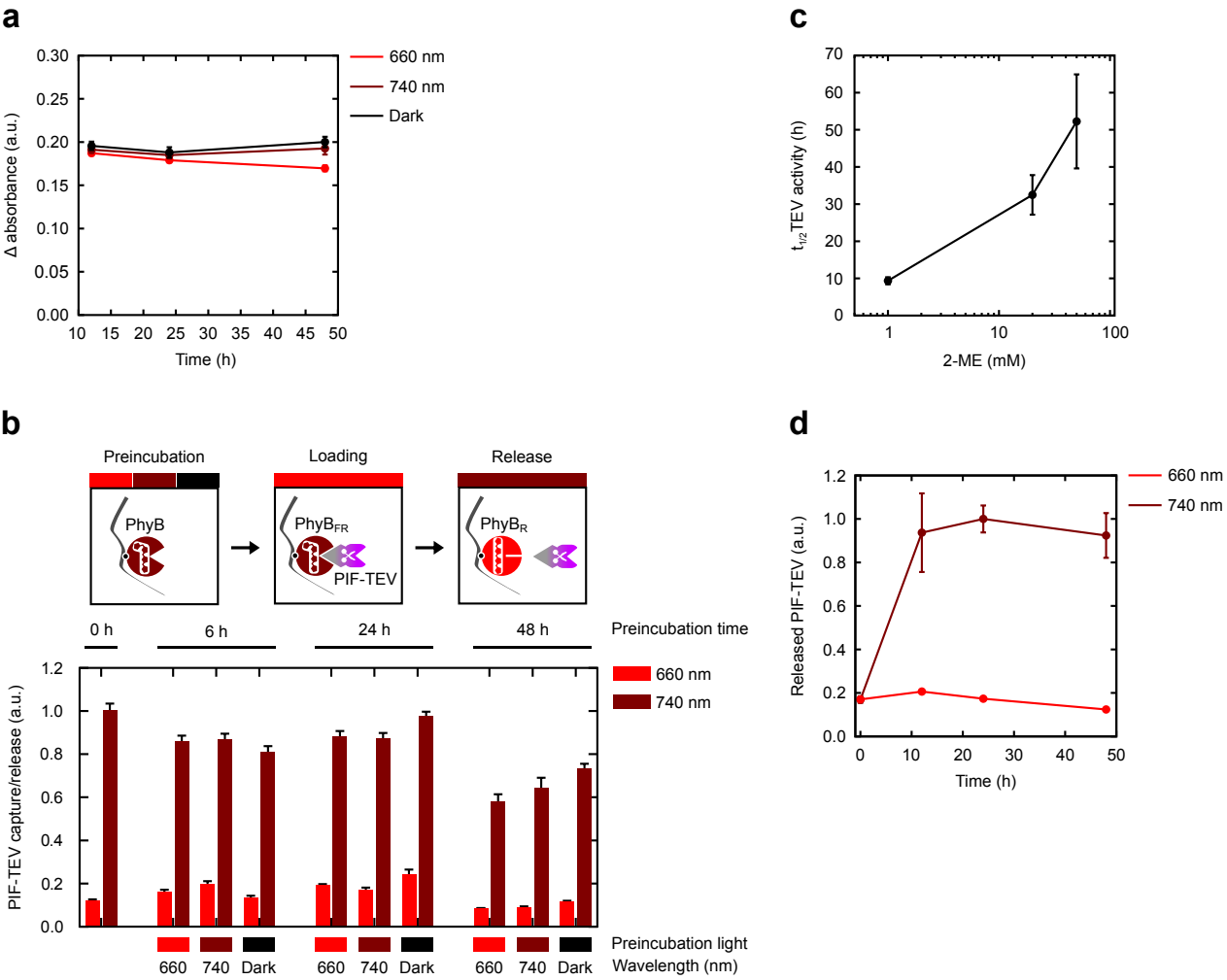

Figure S3. Analysis of the stability of the polymers. **a**, Evaluation of the photostability of PhyB. PhyB-AviTag (7 µM) was incubated at RT and room atmosphere under 660 nm light, 740 nm light, or in the dark for a period of 48 h. At 12 h, 24 h, and 48 h difference spectra (740 – 660 nm) were recorded. Shown is the difference of maxima and minima for each difference spectrum. For the sample illuminated with 660 nm light we determined a half-life time of 270.6 ± 75.8 h. For the other samples, no degradation was observed. **b**, Evaluation of the functionality of PhyB under prolonged illumination. To functionally assess the stability of PhyB, biotinylated photoreceptor (2 nmol) was coupled to streptavidin-conjugated agarose polymer and incubated at RT and room atmosphere under the indicated light conditions. Before starting light treatment (0 h) and after 6 h, 24 h, and 48 h samples were loaded with PIF-TEV under 660 nm light for 1 h, washed, and subsequently either kept under 660, or 740 nm light for 1 h to functionally test photoswitching by quantitation of PIF-TEV from the supernatant via mCherry fluorescence. **c**, Evaluation of PIF-TEV stability. TEV protease being a cysteine protease is intrinsically sensitive to oxidation of the thiol group in the active center. Thus, stability can be adjusted by varying the concentration of reducing agents in the buffer. PIF-TEV was incubated at RT and room atmosphere for 24 h in the presence of the indicated initial concentrations of 2-mercaptoethanol (2-ME). TEV activity was tested at 0, 6, and 24 h and the half-life times were calculated. **d**, Evaluation of the stability of the essential interactions accounting for the stability of the materials systems (streptavidin/biotin, PhyB/PIF). PhyB-AviTag (2 nmol) conjugated via the biotin/streptavidin interaction to agarose polymer was loaded with saturating amounts PIF-TEV. The samples were incubated at RT under room atmosphere for 48 h. No increase in released PIF-TEV (quantified via

mCherry fluorescence) was observed under 660 nm light, indicating stability of the PhyB-PIF and biotin-streptavidin bonds. **a-d,** Experiments were performed in assembly buffer, data points are mean values of 4 replicates, error bars represent one standard deviation.

These data indicate that the synthetic biological modules, given appropriate buffer conditions, are sufficiently stable to support functionality of the materials system for extended time scales even under room atmosphere and RT. If extended experiments are required, the light dose may strongly be reduced to limit photodamage to the chromophor. For example, we have shown in previous experiments that a light intensity of 0.2 µmol m^{-2} s^{-1} instead of the 100 µmol m^{-2} s^{-1} as used in this study was sufficient for efficiently switching the PhyB photoreceptor.[11] Additionally, the cysteine protease TEV could be replaced by other specific proteases such as serine- or metallo-proteases that do not require reducing conditions and are stable under room atmosphere.

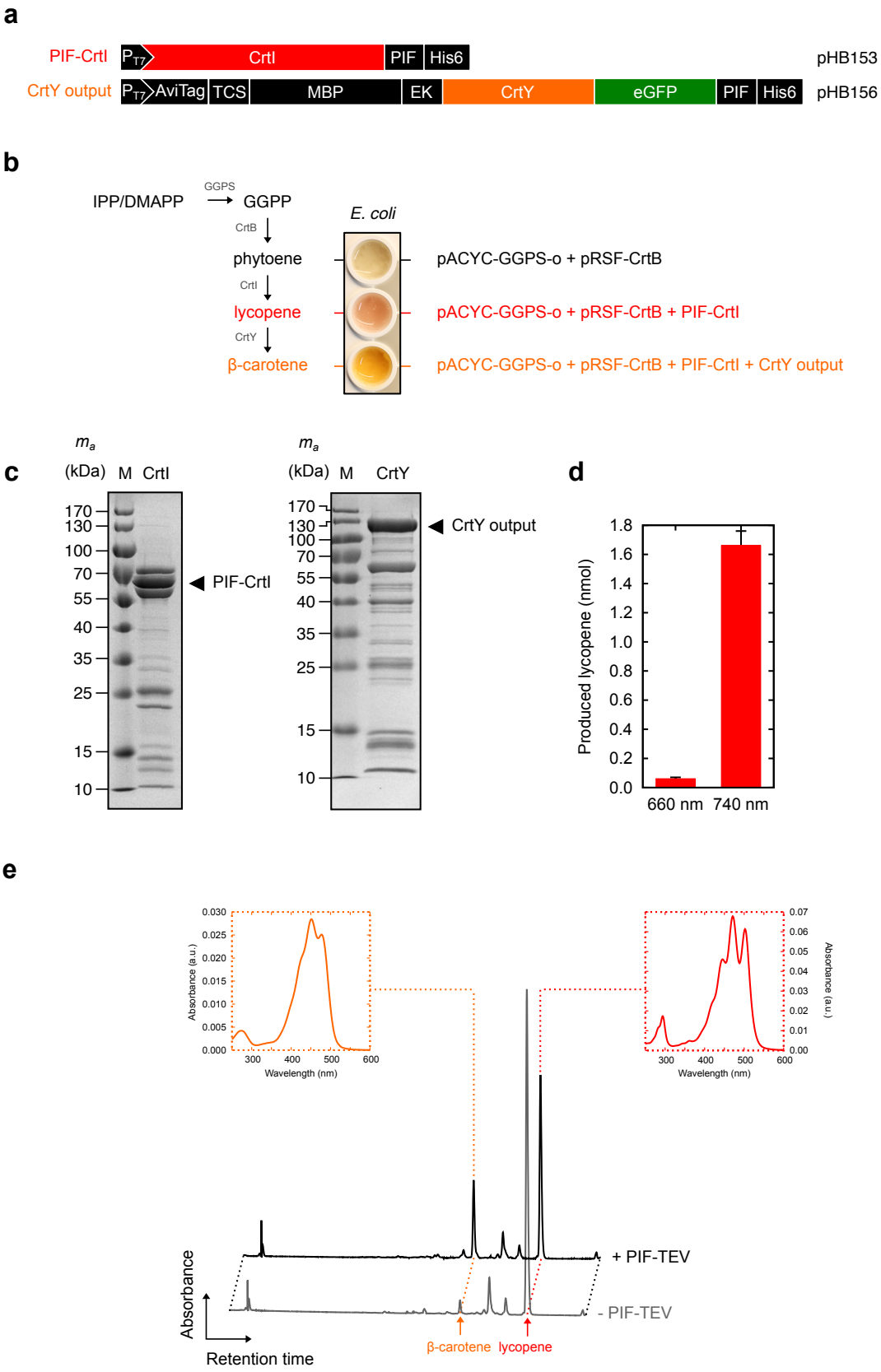

Figure S4. Functional characterization of the modified biocatalysts CrtI (*Pantoea ananatis* phytoene desaturase) and CrtY (*Pantoea ananatis* lycopene cyclase). **a**, Plasmids for the production of the modified enzymes CrtI and CrtY, see Table S1 for full description. **b**, Functional test of the CrtI and CrtY expression plasmids. The CrtI and CrtY-encoding

plasmids (Figure S4a) were tested in an *in vivo* color complementation assay. Phytoene-accumulating *E. coli* BL21 (DE3) cells were generated by co-transformation of the plasmids pACYC-GGPS-o and pRSF-CrtB encoding the enzymes *A. thaliana* geranylgeranyl pyrophosphate synthase 11 (GGPS) and *Pantoea agglomerans* phytoene synthase (CrtB). Red and orange pigment formation was observed upon co-transformation of plasmids encoding PIF-CrtI or PIF-CrtI and CrtY output and induction with 1 mM IPTG at OD_{600} = 0.5 for 6 h. **c**, Coomassie staining of Co^{2+}-NTA purified PIF-CrtI and CrtY output enzymes. **d**, Light-dependent release of CrtI. 2 nmol biotinylated PhyB was added to streptavidin-conjugated agarose suspension and loaded with a saturating amount of PIF-CrtI under 660 nm light. Subsequently, the samples were illuminated with 660 or 740 nm light for 1 h before the enzyme activity was detected in the supernatant by converting phytoene into lycopene. The quantification of lycopene by HPLC is shown. **e**, Functional analysis of purified CrtY output protein. 0.134 nmol of AviTag-TCS-MBP-EK-CrtY-eGFP-PIF was coupled to 20 µL streptavidin-conjugated agarose suspension and incubated for 5 h at room temperature in the presence or absence of 0.22 nmol (15 µg) PIF-TEV. The supernatants were assessed for CrtY activity by measuring the conversion of lycopene into β-carotene. HPLC chromatograms are shown with absorption spectra for all-*trans*-lycopene and all-*trans*-β-carotene. Abbreviations: AviTag, biotinylation motif; CrtI, *Pantoea ananatis* phytoene desaturase; CrtY, *Pantoea ananatis* lycopene cyclase; DMAPP, dimethylallyl pyrophosphate; EK, enterokinase cleavage site; GGP, geranylgeranyl diphosphate; His6, hexahistidine-tag; IPP, isopentenyl pyrophosphate; MBP, maltose-binding protein; PIF, phytochrome interacting factor 6 residues 1-100; TCS, TEV cleavage site.

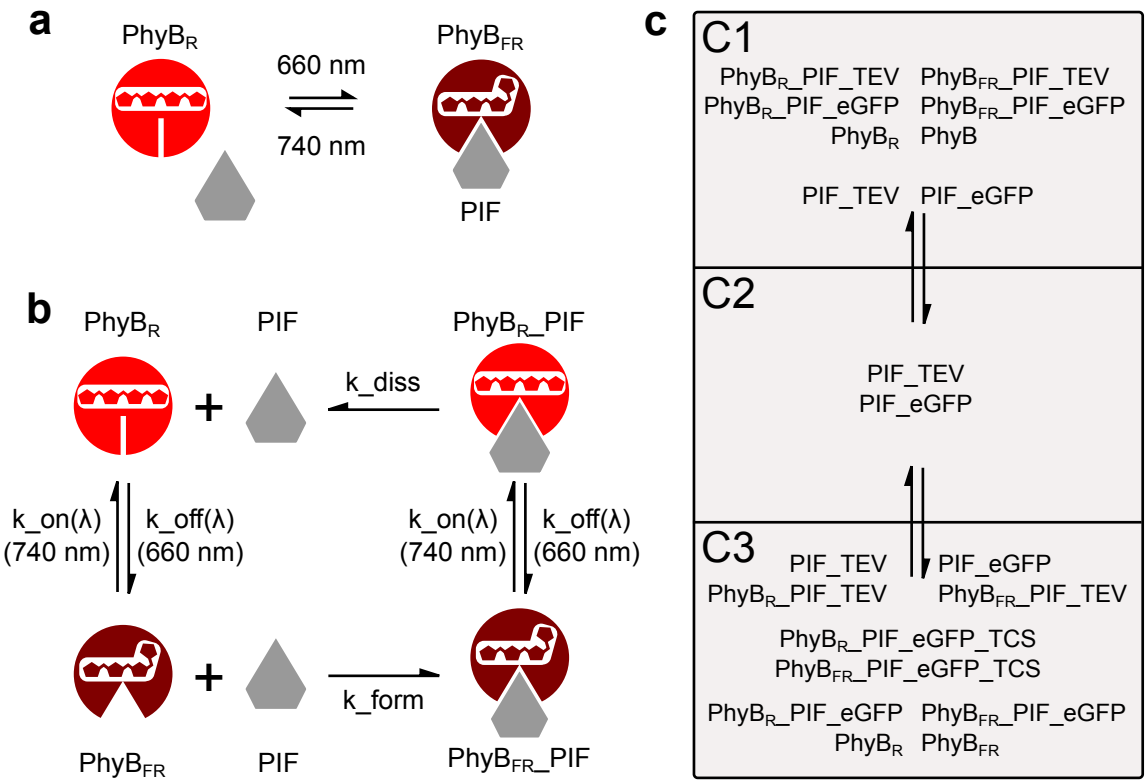

Figure S5. Model scheme. **a**, Simple representation of the PhyB/PIF interaction with only two reactions. The photoreceptor PhyB binds to PIF upon exposure to 660 nm light ($PhyB_{FR}$ form), whereas illumination with 740 nm light shifts the equilibrium to the monomeric form ($PhyB_R$ form). **b**, Detailed core model of the light-induced PhyB/PIF interaction. Illumination with light induces the transition between the $PhyB_{FR}$ and the $PhyB_R$ forms. The rates of this transition depend on the wavelength. PIF can only bind to $PhyB_{FR}$ and dissociates from $PhyB_R$. **c**, To model the spatial effects, three compartments were used. The compartments C1 and C3 contain functional polymer material, whereas compartment C2 contains buffer. Only free PIF-TEV and released output protein (PIF-eGFP) is able to pass between the three compartments.

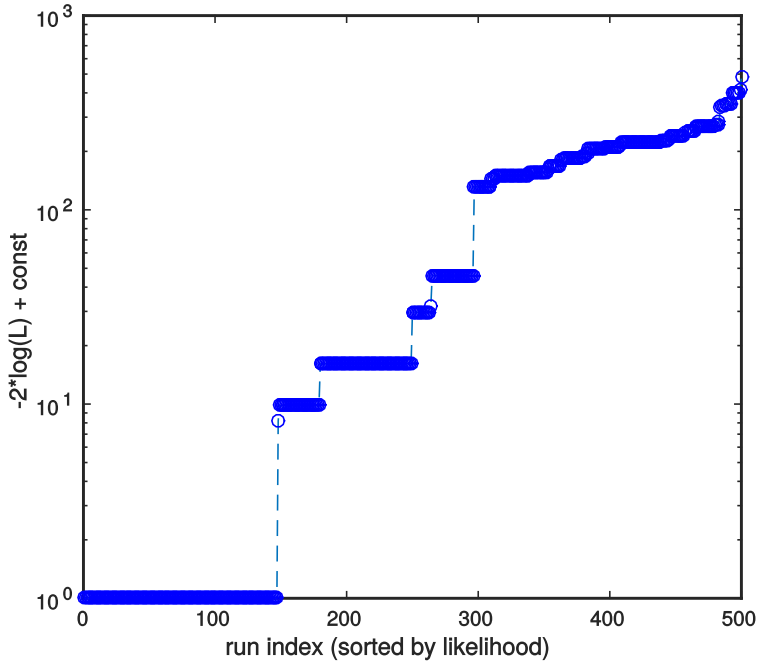

Figure S6. Multiple optimization runs with random initial parameters sorted by the –2 log(L) value. The steps indicate local minima.

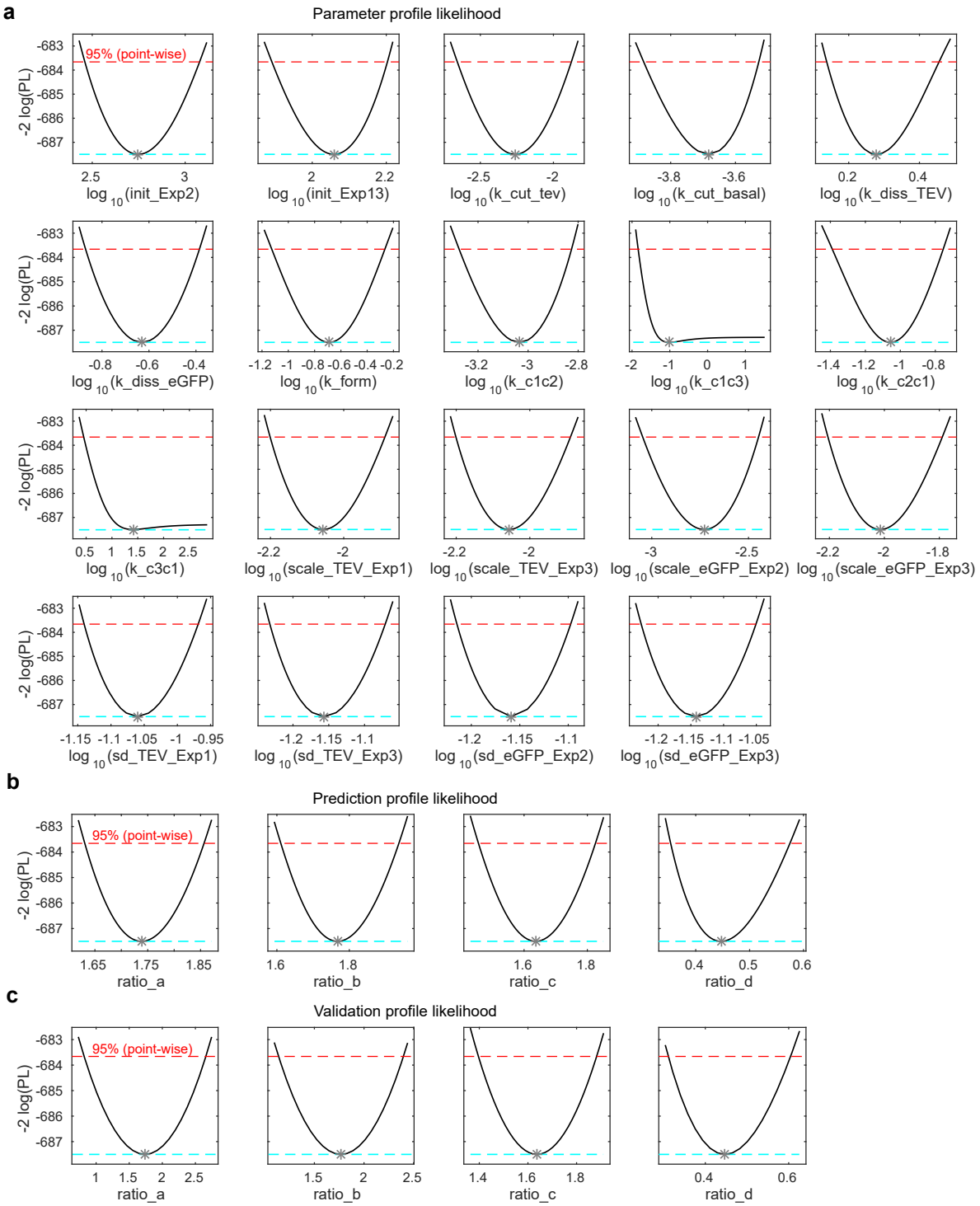

Figure S7. Parameter, prediction and validation profile likelihood of the light pulse-counting materials system. **a**, Profile likelihood of the estimated parameters. The solid lines indicate the profile likelihood, the optimal parameter set is marked with a grey star. The parameter axis is on a logarithmic scale. **b-c**, Prediction profile likelihood (**b**) and validation profile likelihood (**c**) of the ratios in Figure 2e. The solid lines indicate the corresponding profile likelihood and the prediction of the optimal parameter set is marked with a grey star. **a-c**, The red dashed line marks the 95% confidence level. The light blue dashed line indicates the –2log(PL) value of the optimal parameter set.

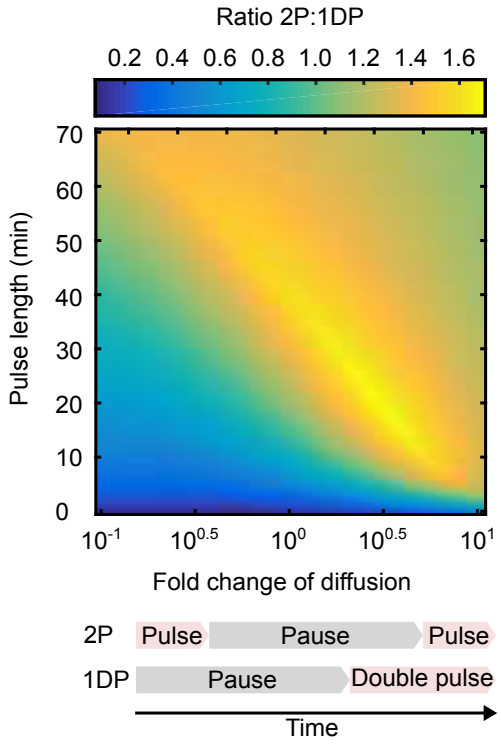

Figure S8. Counting capability of the system as a function of the diffusion speed and the pulse length. The calibrated model was simulated for different pulse lengths and diffusion speeds and the resulting ratio *r* (eq. 1.87), which quantifies the model capability to count, was evaluated. The pause length between two pulses was set to 100 minutes.

Table S1.
Plasmids and oligonucleotides used in this study.

Plasmid	Description	Reference
p83	**$P_{ara/lac}$::Cph1-His6** Bacterial expression vector encoding hexahistidine-tagged *Synechocystis* phytochrome Cph1Δ2.	Essen *et al.* [12]
p171	Bicistronic bacterial expression vector for *Synechocystis* heme oxygenase (HO1) and phycocyanobilin:ferredoxin oxidoreductase (PcyA).	Essen *et al.* [12]
pACYC-GGPS-o	**P_{T7}::GGPS** Bacterial expression vector encoding untagged *A. thaliana* geranylgeranyl diphosphate synthase 11 (NCBI Accession: NM_119845.3).	unpublished
pAL149	**P_{CMV}::PhyB(N908)-10aaLinker-mCherry-Kras4BCT-pA** Plasmid encoding *A. thaliana* Phytochrome B (NCBI Accession: NM_127435.3).	Levskaya *et al.* [13]
pBirACm	**P_{tac}::BirA** IPTG-inducible bacterial expression plasmid for the biotin ligase BirA.	Avidity, LLC
pCDF-CrtI-o	**P_{T7}::CrtI** Bacterial expression vector encoding untagged *Pantoea ananatis* phytoene desaturase CrtI (NCBI Accession: D90087.2).	unpublished
pCrtY-HMGWA	**P_{T7}::His6-MBP-EK-CrtY** Bacterial expression vector encoding hexahistidine-tagged and MBP-fused *Pantoea ananatis* lycopene cyclase CrtY harboring an enterokinase cleavage site.	Yu et al. [2]
pHB002	**P_{T7}::MBP-TCS-His6-TEV-mCherry-PIF6(amino acids 1-100, designated as APB)** MBP-H6-TEV was amplified from pRK793 using oligonucleotides oHB001 (5'-GAAATAATTTTG-TTTAACTTTAAGAAGGAGATATACATATGAAAATCGAAGAAGGTAAACTGGTAATCTGG-3') and oHB002 (5'-GCTCACCATGCCAGAACCGCTACCTGCACCGCTCGAATTCATGAGTTGAG-TCGCTTCCTTAACTGG-3'). mCherry-PIF6(APB) was amplified from pMH023 using oHB003 (5'-TCGAGCGGTGCAGGTAGCGG-3') and oHB005 (5'-CTTCCTTTCGGGCTTTGTTAGCAGC-CGGATCAAGCTTTTAGTCAACATGTTTATTGCTTTCCAACATGTTTGTTTC-3'). Products were Gibson-cloned [14] into *Hin*dIII/*Nde*I digested pWW301.	This work
pHB004	**P_{T7}::AviTag-TCS-eGFP-PIF6(APB)** eGFP carrying the monomerizing A206K mutation was amplified from pMZ725 using oligonucleotides oHB006 (5'-CGAAGGCGGCAGCGCGGGCAGCGGTAGGAGCGGCGAAAATCTTTATT-TTCAAGGTAGCGGCGGTAGCGGCGCGGAAAGCGGTGGCATGGTGAGCAAGGGCGAGGA-GC-3') and oHB008 (5'-AGCAGAACCTGCGGAGCCCTTGTACAGCTCGTCCATGCCGAG-3').	This work

Plasmid	Description	Reference
	The additional sequence was attached using oHB007 (5'-GAAATAATTTTGTTTAACTTTAAGA-AGGAGATATACATATGTCCGGCCTGAACGACATCTTCGAGGCTCAGAAAATCGAATGGCA-CGAAGGCGGCAGCGCGG-3') and oHB008. PIF6(APB) was amplified from pMH023 using oHB009 (5'-ATGGACGAGCTGTACAAGGGCTCCGCAGGTTCTGCTGGT-3') and oHB011 (5'-CTTCCTTTCGGGCTTTGTTAGCAGCCGGATCAAGCTTTTAATGGTGATGGTGATGATGGTC-AACATGTTTATTG-3'). All PCR products were Gibson-cloned into *Hin*dIII/*Nde*I digested pWW301.	
pHB153	**P_{T7}::CrtI-PIF6(APB)** CrtI was PCR amplified from pCDF-CrtI-o using the oligonucleotides oHB642F (5'-GAGCGGAT-AACAATTCCCCTGTAGAAATAA-3') and oHB643R (5'-AGCAGAACCTGCGGAGCCAATCAGA-TCCTCCAGCATCAAACCTG-3'). PIF6(APB) was amplified from pHB004 using oHB644F (5'-A-TGCTGGAGGATCTGATTGGCTCCGCAGGTTCTGCTG-3') and oHB645R (5'-ACAATACGAT-TACTTTCTGTTCGACTTAAGCATTATGCGGCCGCTTAATGGTGATGGTGATGATGGTCAAC-ATG-3'). The products were Gibson-cloned into *Not*I/*Nco*I digested pCDFDuet.	This work
pHB156	**P_{T7}::AviTag-TCS-MBP-EK-CrtY-eGFP-PIF6-His6** AviTag-TCS was PCR amplified from pHB004 using oligonucleotides oHB654F (5'-CTAGAAAT-AATTTTGTTTAACTTTAAGAAGGAGATATACCATGTCCGGCCTGAACGACATC-3') and oHB655R (5'-TTCTTCAGTTTTGGTACCGCCACCGCTTTCCGCGC-3'). MBP-EK-CrtY was amplified from pCrtY-HMGWA using oHB656F (5'-GGCGCGGAAAGCGGTGGCGGTACCAAA-ACTGAAGAAGGTAAACTGGTAATC-3') and oHB657R (5'-GCCAGAACCGCTACCTGCACCG-CTCGATCCTTTATCTCGTCTGTCAGGAAAATGG-3'). Monomerized eGFP-PIF6(APB) was amplified from pHB004 using oHB658F (5'-GATAAAGGATCGAGCGGTGCAGGTAGCGGTTCT-GGCATGGTGAGCAAGGGCGAGGAG-3') and oHB659R (5'-GTTAGCAGCCGGATCTCAGTG-GTGGTGGTGGTGGTGCTCGAGGTCAACATGTTTATTGCTTTCCAACATGTTTG-3'). The products were Gibson-cloned into *Xho*I/*Nco*I digested pCrtY-HMGWA.	This work
pMH017	**$P_{ara/lac}$::PhyB(N651)-AviTag-His6** Phytochrome B (PhyBN651) was PCR amplified from plasmid pAL149 using oligonucleotides oMH1 (5'-TTCCGAATTCATTAAAGAGGAGAAATTAACTATGGTTTCCGGAGTCGGGGGTAG-3') and oMH38 (5'-TGACGCGGCCGCTTAATGGTGATGGTGATGATGTTCGTGCCATTCGATT-TTCTGAGCTTCGAAGATGTCGTTCAGACCGCTACCAGAACCTGCACCTAACTCATCAATCC-CCTG-3') followed by subsequent cloning into *Not*I/*Eco*RI digested p83.	Smith *et al.* [15]
pMH023	**P_{T7}::ZZ-mCherry-PIF6(APB)-His6** Plasmid encoding a hexahistidine-tagged fusion protein comprising the Fc-binding ZZ domain of protein A, mCherry and the APB domain of PIF6.	unpublished
pMZ725	**P_{SV40}::PIF3-eGFP-pA**	Beyer *et al.* [11]

Plasmid	Description	Reference
	Mammalian expression vector encoding *A. thaliana* phytochrome interacting factor 3 (PIF3) and eGFP-A206K.	
pRK793	**P_{T7}::MBP-TCS-His6-TEV** Bacterial expression plasmid encoding MBP-fused TEV(S219V) protease.	Kapust *et al.* [16]
pRSF-CrtB	**P_{T7}::His6-CrtB** Bacterial expression vector encoding hexahistidine-tagged *Pantoea agglomerans* phytoene synthase (CrtB, NCBI Accession: M38423.1).	unpublished
pWW301	**P_{T7}::ET1-His6** A pRSET-derived bacterial expression vector for the macrolide-responsive transactivator ET1.	Weber *et al.* [17]

Table S2.
Production and purification of recombinant proteins.

Plasmid	Protein	Host	Temp	Medium	Induction	Density	Duration	Resin
pHB002	PIF-mCherry-TEV	*E. coli* BL21 (DE3) pLysS	11 °C	LB	1 mM IPTG	OD_{600} = 0.8	18 h	Ni^{2+}-NTA
pHB004	AviTag-TCS-eGFP-PIF	*E. coli* BL21 (DE3) pBirACm	30 °C	LB	1 mM IPTG, 50 µM biotin	OD_{600} = 0.6	6 h	Ni^{2+}-NTA
pHB153	CrtI-PIF	*E. coli* BL21 (DE3)	15 °C	2xYT	1 mM IPTG	OD_{600} = 0.5	18 h	Co^{2+}-NTA
pHB156	AviTag-TCS-MBP-CrtY-eGFP-PIF	*E. coli* BL21 (DE3) pBirACm	28 °C	LB	1 mM IPTG, 50 µM biotin	OD_{600} = 0.8	6 h	Co^{2+}-NTA
pMH017	PhyB	*E. coli* BL21 (DE3) p171	18 °C	LB	1 mM IPTG, 0.4% (w/v) arabinose, 50 µM biotin	OD_{600} = 0.8	20 h	Ni^{2+}-NTA

Table S3.
Fitted parameter values obtained by maximum likelihood estimation. σ^- and σ^+ indicate the 95% point-wise confidence intervals calculated by exploring the profile likelihood.

Parameter	$\hat{\theta}$	σ^-	σ^+	Unit
k_{cut_tev}	$5.47 \cdot 10^{-03}$	$2.20 \cdot 10^{-03}$	$1.22 \cdot 10^{-02}$	$nM^{-1} \cdot min^{-1}$
k_{cut_basal}	$2.08 \cdot 10^{-04}$	$1.31 \cdot 10^{-04}$	$2.97 \cdot 10^{-04}$	min^{-1}
k_{diss_TEV}	$1.90 \cdot 10^{+00}$	$1.37 \cdot 10^{+00}$	$2.85 \cdot 10^{+00}$	min^{-1}
k_{diss_eGFP}	$2.34 \cdot 10^{-01}$	$1.35 \cdot 10^{-01}$	$4.12 \cdot 10^{-01}$	min^{-1}
k_{form}	$2.04 \cdot 10^{-01}$	$7.48 \cdot 10^{-02}$	$5.43 \cdot 10^{-01}$	$nM^{-1} \cdot min^{-1}$
$k_{\_c2c1}$	$9.23 \cdot 10^{-04}$	$5.30 \cdot 10^{-04}$	$1.49 \cdot 10^{-03}$	min^{-1}
$k_{\_c1c2}$	$8.78 \cdot 10^{-02}$	$4.08 \cdot 10^{-02}$	$1.76 \cdot 10^{-01}$	min^{-1}
$k_{\_c2c3}$	$9.79 \cdot 10^{-02}$	$1.45 \cdot 10^{-02}$	+ inf	min^{-1}
$k_{\_c3c2}$	$2.56 \cdot 10^{+01}$	$2.84 \cdot 10^{+00}$	+ inf	min^{-1}
$init_{Exp2}$	$5.59 \cdot 10^{+02}$	$2.89 \cdot 10^{+02}$	$1.20 \cdot 10^{+03}$	nM
$init_{Exp13}$	$1.14 \cdot 10^{+02}$	$7.78 \cdot 10^{+01}$	$1.60 \cdot 10^{+02}$	nM
$scale_{eGFP\_Exp2}$	$1.87 \cdot 10^{-03}$	$8.98 \cdot 10^{-04}$	$3.56 \cdot 10^{-03}$	$NFU^* \cdot nM^{-1}$
$scale_{eGFP\_Exp3}$	$9.67 \cdot 10^{-03}$	$6.23 \cdot 10^{-03}$	$1.63 \cdot 10^{-02}$	$NFU \cdot nM^{-1}$
$scale_{TEV\_Exp1}$	$8.79 \cdot 10^{-03}$	$6.30 \cdot 10^{-03}$	$1.30 \cdot 10^{-02}$	$NFU \cdot nM^{-1}$
$scale_{TEV\_Exp3}$	$8.77 \cdot 10^{-03}$	$6.29 \cdot 10^{-03}$	$1.29 \cdot 10^{-03}$	$NFU \cdot nM^{-1}$
sd_{eGFP_Exp2}	$6.94 \cdot 10^{-02}$	$6.10 \cdot 10^{-02}$	$7.99 \cdot 10^{-02}$	NFU
sd_{eGFP_Exp3}	$7.20 \cdot 10^{-02}$	$5.94 \cdot 10^{-02}$	$8.90 \cdot 10^{-02}$	NFU
sd_{TEV_Exp1}	$8.70 \cdot 10^{-02}$	$7.24 \cdot 10^{-02}$	$1.07 \cdot 10^{-01}$	NFU
sd_{TEV_Exp3}	$6.97 \cdot 10^{-02}$	$5.86 \cdot 10^{-02}$	$8.48 \cdot 10^{-02}$	NFU

* NFU = Normalized fluorescence units

Table S4.
Predicted ratios, prediction confidence intervals (CI) and validation confidence intervals of the measured points in Figure 2e.

Point in Figure 2e	Predicted ratio	Lower bound of prediction CI	Upper bound of prediction CI	Lower bound of validation CI	Upper bound of validation CI
A	1.74	1.63	1.86	0.82	2.66
B	1.77	1.61	1.94	1.14	2.40
C	1.64	1.46	1.83	1.40	1.88
D	0.45	0.34	0.59	0.31	0.61

Table S5.
Measurements of the ratios in Figure 2e with the propagated standard error of the mean.

Point in Figure 2e	Pulse duration	Pause between two pulses	Mean of measured triplicates	Standard error of the mean
A	40	200	2.28	0.31
B	30	300	2.11	0.47
C	20	400	1.59	0.08
D	20	20	0.33	0.03

Supporting References

[1] P. Schaub, Q. Yu, S. Gemmecker, P. Poussin-Courmontagne, J. Mailliot, A. G. McEwen, S. Ghisla, S. Al-Babili, J. Cavarelli, P. Beyer, *PLoS One* **2012**, *7*, e39550.

[2] Q. Yu, P. Schaub, S. Ghisla, S. Al-Babili, A. Krieger-Liszkay, P. Beyer, *J. Biol. Chem.* **2010**, *285*, 12109.

[3] A. L. Mancinelli, in *Photomorphogenes. Plants*, Springer Netherlands, Dordrecht, **1994**, pp. 211–269.

[4] A. Raue, C. Kreutz, T. Maiwald, J. Bachmann, M. Schilling, U. Klingmuller, J. Timmer, *Bioinformatics* **2009**, *25*, 1923.

[5] A. Raue, B. Steiert, M. Schelker, C. Kreutz, T. Maiwald, H. Hass, J. Vanlier, C. Tönsing, L. Adlung, R. Engesser, W. Mader, T. Heinemann, J. Hasenauer, M. Schilling, T. Höfer, E. Klipp, F. Theis, U. Klingmüller, B. Schöberl, J. Timmer, *Bioinformatics* **2015**, *31*, btv405.

[6] A. C. Hindmarsh, P. N. Brown, K. E. Grant, S. L. Lee, R. Serban, D. E. Shumaker, C. S. Woodward, *ACM Trans. Math. Softw.* **2005**, *31*, 363.

[7] T. F. Coleman, Y. Li, *SIAM J. Optim.* **1996**, *6*, 418.

[8] A. Raue, V. Becker, U. Klingmüller, J. Timmer, *Chaos* **2010**, *20*, 45105.

[9] C. Kreutz, A. Raue, J. Timmer, *BMC Syst. Biol.* **2012**, *6*, 120.

[10] H. Hass, C. Kreutz, J. Timmer, D. Kaschek, *Bioinformatics* **2015**, *32*, 1204.

[11] H. M. Beyer, S. Juillot, K. Herbst, S. L. Samodelov, K. Müller, W. W. Schamel, W. Römer, E. Schäfer, F. Nagy, U. Strähle, W. Weber, M. D. Zurbriggen, *ACS Synth. Biol.* **2015**, *4*, 951.

[12] L.-O. Essen, J. Mailliet, J. Hughes, *Proc. Natl. Acad. Sci. U. S. A.* **2008**, *105*, 14709.

[13] A. Levskaya, O. D. Weiner, W. A. Lim, C. A. Voigt, *Nature* **2009**, *461*, 997.

[14] D. G. Gibson, L. Young, R.-Y. Chuang, J. C. Venter, C. A. Hutchison, H. O. Smith, *Nat. Methods* **2009**, *6*, 343.

[15] R. W. Smith, B. Helwig, A. H. Westphal, E. Pel, M. Hörner, H. M. Beyer, S. L. Samodelov, W. Weber, M. D. Zurbriggen, J. W. Borst, C. Fleck, *BMC Syst. Biol.* **2016**, *10*, 110.

[16] R. B. Kapust, J. Tözsér, J. D. Fox, D. E. Anderson, S. Cherry, T. D. Copeland, D. S. Waugh, *Protein Eng.* **2001**, *14*, 993.

[17] C. C. Weber, N. Link, C. Fux, A. H. Zisch, W. Weber, M. Fussenegger, *Biotechnol. Bioeng.* **2005**, *89*, 9.